

Interferometric Estimation of Three-Dimensional Ice-Flow Using Ascending and Descending Passes

Ian R. Joughin, *Member, IEEE*, Ronald Kwok, *Member, IEEE*, and Mark A. Fahnestock

Abstract—Satellite radar interferometry (SRI) provides an important new tool for determining ice-flow velocity. Interferometric measurements made from a single-track direction are sensitive only to a single component of the three-component velocity vector. Observations from along three different track directions would allow the full velocity vector to be determined. A north/south-looking synthetic aperture radar (SAR) could provide these observations over large portions of the globe, but not over large areas of the polar ice sheets. We develop and demonstrate a technique that allows the three-component velocity vector to be estimated from data acquired along two track directions (ascending and descending) under a surface-parallel flow assumption. This technique requires that we have accurate estimates of the surface slope, which we also determined interferometrically. To demonstrate the technique, we estimate the three-component velocity field for the Ryder Glacier, Greenland. Our results are promising, although we do not have yet ground-truth data with which to determine the accuracy of our estimates.

Index Terms—Interferometry, remote sensing, synthetic aperture radar (SAR).

I. INTRODUCTION

AN UNDERSTANDING of the flow dynamics of an ice sheet's outlet glaciers and ice streams requires knowledge of their flow velocity and strain rates (i.e., velocity gradients). With the advent of the Global Positioning System (GPS), glaciologists now are able to make precise *in situ* estimates of ice-flow velocity. While highly accurate, it is time consuming and logistically difficult to make such measurements. After a long field season, a glaciologist is likely to have measured velocity at only a few dozen points. Ice-flow velocity also has been measured from the displacement of features observed in pairs of visible [1] or synthetic aperture radar (SAR) images [2], but these methods do not work well for the large, featureless areas that comprise much of the ice sheets.

Manuscript received October 21, 1996; revised April 28, 1997. The work of I. R. Joughin and R. Kwok was performed at the Jet Propulsion Laboratory, California Institute of Technology, Pasadena, CA, under contract with National Aeronautics and Space Administration (NASA). M. Fahnestock was supported under NASA NMTPE Grant NAGW4285. SAR data were provided by the European Space Agency.

I. R. Joughin and R. Kwok are with the Jet Propulsion Laboratory, California Institute of Technology, Pasadena, CA 91109 USA (e-mail: ian@rgps1.jpl.nasa.gov).

M. A. Fahnestock is with the Joint Center for Earth System Science, Department of Meteorology, University of Maryland, College Park, MD 20742 USA.

Publisher Item Identifier S 0196-2892(98)00224-1.

Thus, the need for detailed ice-flow velocity measurements over wide areas has not been met by conventional techniques.

Since the launch of ERS-1, the capability of satellite radar interferometry (SRI) data for making detailed ice-flow measurements has been firmly established [3]–[15]. The measurement of ice motion by using SRI was first demonstrated by Goldstein *et al.* [3] for an area on the Rutford Ice Stream, Antarctica. Hartl *et al.* [4] have used ERS interferometry to study tidal displacement on the Filchner–Ronne Ice Shelf. Kwok and Fahnestock [5] measured relative velocities on the North-East Greenland Ice Stream. Joughin *et al.* [6]–[9] have mapped topography and measured absolute velocities in Greenland and detected a mini-surge [10]. Rignot *et al.* have used ERS-1 interferometry to measure ice velocity [11], grounding-line position [12], tidal flexure [12] in Greenland, and SIR-C interferometry to study topography and ice motion on the San Rafael Glacier, Chile [13]. Fatland [15] has made SRI velocity measurements on Alaskan Glaciers, and Vachon *et al.* [14] have used interferometry to study Canadian glaciers.

Previous studies [3]–[14] have relied on images collected along a single satellite track. A repeat-pass interferometer, however, is sensitive only to surface displacement that is directed along the line of sight from the radar to the ground. As a result, interferograms acquired along a single track are sensitive to displacement along a single direction, which for ERS-1/2 emphasizes vertical displacement relative to horizontal displacement [6]. Furthermore, without additional information, it is not possible to unambiguously separate the mixed horizontal and vertical displacement signals in an interferogram. In this paper, we derive a technique for estimating all three components of the ice-flow velocity vector by using two nonparallel tracks (i.e., ascending and descending tracks) and surface slope from interferometry.

We begin with a brief review of interferometry followed by a derivation of the technique for three-component velocity determination. We then apply the technique to estimate the three-component velocity vector for an area over the ice sheet and the Ryder Glacier, Greenland. Next, we discuss the limitations and sources of error in the technique. Finally, we discuss the current limitations to, and future application of, the technique.

II. INTERFEROMETRY BACKGROUND

A. Interferometer Geometry

The geometry of an interferometric SAR is shown in Fig. 1. The interferometer acquires two images of the same scene with

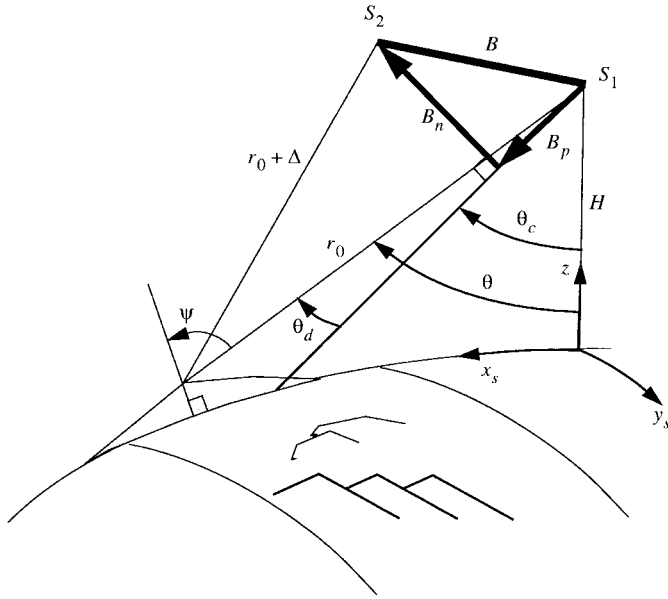


Fig. 1. Geometry of an interferometric SAR.

SAR's located at S_1 and S_2 . The first SAR is at altitude H and is travelling in the y_s direction. From S_1 , the look angle θ and the slant range r_0 are determined by a point-ground range x_s and elevation z above some reference ellipsoid. The range to the same point from the SAR at S_2 differs from r_0 by Δ . For a single-pass system, such as TOPSAR [16], two images are acquired simultaneously by using separate antennas. A repeat-pass interferometer, on the other hand, acquires a single image of the same area twice from two nearly repeating orbits or flight lines. Repeat-pass interferometry is examined in this paper since single-pass interferometry is not sensitive to surface displacement.

The baseline separating the SAR's can be expressed in terms of its components normal to B_n and parallel to B_p , a reference-look direction. A convenient choice is to let the nominal-center look angle θ_c define the reference-look direction. The angle θ_d then denotes the deviation of θ from θ_c .

B. Interferometric Phase

For repeat-pass interferometry, the range difference between passes is estimated by using

$$\hat{\Delta} = \frac{\phi_{\text{unwrap}}}{2k} = \frac{\lambda}{4\pi} \phi_{\text{unwrap}} \quad (1)$$

where ϕ_{unwrap} denotes the unwrapped interferometric-phase difference and λ is the radar wavelength. Note that phase-unwrapping algorithms, which are used to remove the mod- 2π ambiguity in the interferometric phase, yield only the relative phase as there is an unknown constant of integration associated with the unwrapped solution [17]. It is assumed here that ϕ_{unwrap} has been processed to remove this ambiguity [8] (i.e., with the aid of tie points). The ERS-1 SAR operates at a wavelength of $\lambda = 5.656$ cm so that Δ typically can be measured with subcentimeter accuracy.

With a repeat-pass interferometer, Δ is affected by both topography and any movement of the surface between orbits

that is directed toward or away from the look direction of the radar. Therefore, the interferometric phase can be expressed as the sum of displacement- and topography-dependent terms,

$$\phi_{\text{unwrap}} = \phi_{\text{topography}} + \phi_{\text{displacement}} \quad (2)$$

The interferometric phase is also affected by noise, due to speckle and propagation delays caused by atmospheric variation between passes.

C. Effect of Topography

Referring to Fig. 1, the baseline and range difference due to topography $\Delta_{\text{topography}}$ are related by

$$\begin{aligned} B_n \sin \theta_d + B_p \cos \theta_d \\ = -\Delta_{\text{topography}} - \frac{\Delta_{\text{topography}}^2}{2r_0} + \frac{B^2}{2r_0}. \end{aligned} \quad (3)$$

Applying (1) and (3) the phase due topography is solved for as

$$\begin{aligned} \phi_{\text{topography}} \\ = 2k \left[-r_0 + \sqrt{r_0^2 - 2r_0(B_n \sin \theta_d + B_p \cos \theta_d) + B^2} \right] \\ \approx -2k \left(B_n \sin \theta_d + B_p \cos \theta_d - \frac{B^2}{2r_0} \right). \end{aligned} \quad (4)$$

D. Effect of Displacement

The contribution to the phase from surface displacement Δ_d is given by

$$\phi_d = 2k(\Delta_{d,x_s} \sin \psi - \Delta_{d,z} \cos \psi) \quad (5)$$

where Δ_{d,x_s} denotes the component of displacement tangential to the surface of a reference ellipsoid and directed across track, and $\Delta_{d,z}$ denotes displacement directed normal to the ellipsoid. The incidence angle, ψ , is defined with respect to the local normal to the ellipsoid (see Fig. 1). For steady motion, the phase is related to the surface velocity by

$$\phi_d = 2k\delta T(v_{x_s} \sin \psi - v_z \cos \psi) \quad (6)$$

where δT is the time between acquisition of images.

E. Baseline Model and Estimation

ERS-1 orbits are not known well enough to estimate baselines with the level of accuracy needed to generate DEM's and estimate motion [18]. As a result, the baseline must be determined using tie points [9], [18]. The baseline varies along the satellite track, which we model as a linear function of the along-track coordinate, y_s [9]. The baseline is then represented as

$$\begin{aligned} B_n &= B_n^c + \delta B_n \left(\frac{y_s - y_{s,c}}{L_{y_s}} \right) \\ B_p &= B_p^c + \delta B_p \left(\frac{y_s - y_{s,c}}{L_{y_s}} \right) \end{aligned} \quad (7)$$

where B_n^c and B_p^c are the components of baseline at the frame center $y_{s,c}$ and δB_n and δB_p are the changes in the baseline components over the length of the frame L_{y_s} .

With a linear model for baseline variation, there are four unknown parameters: B_n^c , B_p^c , δB_n , δB_p . There is also an unknown constant associated with the phase after it has been unwrapped. We make an approximation to implicitly incorporate this constant into the baseline solution so that only the four baseline parameters need to be determined [8]. We then estimate the baseline using a linear least-squares solution [8], [19] with at least four tie points.

Even if the baseline were determined perfectly (i.e., so that the baseline estimate contributes no error to the velocity estimate), the estimated baseline would differ slightly from the actual baseline. This is because approximations in the baseline model and errors in some of the independent parameters (i.e., satellite altitude) are compensated for by using an effective rather than exact baseline. The difference between the true and effective baseline length is small (i.e., less than a meter).

III. ESTIMATION OF 3-D ICE-FLOW VELOCITY

A. Surface-Parallel Flow Assumption

For ice-dynamics studies we wish to measure the three-component velocity vector

$$\mathbf{v} = v_x \hat{\mathbf{x}} + v_y \hat{\mathbf{y}} + v_z \hat{\mathbf{z}} = \mathbf{v}_h + v_z \hat{\mathbf{z}}. \quad (8)$$

The line-of-sight observation made from along a single track yields only one velocity component. Thus, three interferometric observations from linearly independent directions are necessary to fully resolve the velocity vector. Observations from four directions can be made with a SAR that has north/south-looking capability (i.e., north/south ascending and north/south descending). ERS-1/2 are only able to look north. Furthermore, it is not possible to obtain north- and south-looking coverage at high latitudes, including large parts of Antarctica. Therefore, it is desirable to have the ability to measure the velocity vector with less than three directions of observation.

If we make the assumption that surficial ice is constrained to flow parallel to the ice-sheet surface $z_t(x, y)$, then vertical velocity is related to horizontal velocity by

$$v_z = [\nabla_{xy} z_t(x, y)]^T \mathbf{v}_h. \quad (9)$$

Substituting this expression into (8) yields

$$\mathbf{v} = \mathbf{v}_h + [\nabla_{xy} z_t(x, y)]^T \mathbf{v}_h \hat{\mathbf{z}} \quad (10)$$

which allows the velocity vector to be determined using observations from just two different directions when the surface slope is known. This means that crossing ascending and descending ERS orbits are suitable for estimating the ice-flow velocity vector.

In general ice does not flow parallel to the surface. Instead, ice flow is inclined slightly upward from the surface in the ablation zone (areas of net ice loss) and is tipped slightly downward in the accumulation zone [20]. This deviation from surface-parallel flow, which is called the submergence/emergence velocity, allows the ice sheet to maintain its steady-state shape by making way (submergence) for new snow in the accumulation zone and by replacing

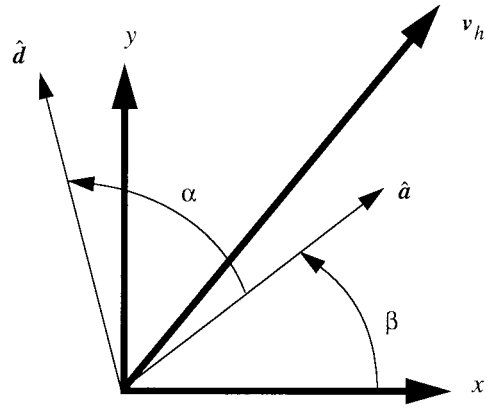


Fig. 2. Vectors and angles used in determining ice-flow velocity.

(emergence) ice lost in the ablation zone. In steady state, the submergence/emergence velocity is equal to the local mass balance, which is a few decimeters to a few meters per year for most of Greenland. In fast moving areas with bumpy terrain, the vertical-component of motion due to surface-parallel flow is large with respect to the submergence/emergence velocity. In areas where there is heavy ablation or accumulation the surface-parallel flow assumption may yield significant errors in estimates of vertical motion. Estimates of the horizontal components of motion should be relatively unaffected by deviations from surface-parallel flow.

Note that if the direction of the velocity vector is known, it is possible to solve for the velocity vector using only a single pass and the surface parallel flow assumption [9]. Flow direction can be estimated from the direction of maximum averaged (i.e., over 10–20 ice thicknesses) downhill slope [20]. This yields an averaged flow direction, however, that misses perturbations in the direction of flow on scales of less than a few ice thicknesses (i.e., 1–10 km). Flow direction can also be inferred from features in visible in the amplitude imagery such as shear margins and flow stripes. Most SAR amplitude images of the ice sheet are relatively featureless, so that it is possible to determine flow direction for only a few regions within an image. Furthermore, a single interferogram also has sensitivity to one component of the horizontal flow vector. As a result, it is possible only to make accurate measurements over a range of directions where there is good sensitivity to displacement. For these reasons it is desirable estimate velocity using both ascending and descending passes whenever possible.

B. Estimation of Velocity Vector Under the Surface-Parallel Flow Assumption

In this section we derive the equations necessary to estimate the ice-flow velocity vector from two nonparallel (i.e., ascending and descending) tracks under the surface-parallel flow assumption. We begin by defining a three-dimensional (3-D), right-handed, xyz -coordinate system with some arbitrary orientation of the xy axes in the plane tangential to a reference ellipsoid (Fig. 2).

Let $\hat{\mathbf{a}}$ and $\hat{\mathbf{d}}$ be the unit vectors corresponding to the across-track directions of the ascending and descending passes, respectively. The angular separation of tracks is denoted by

α (Fig. 2). The across-track vectors form a nonorthonormal basis, allowing the horizontal velocity vector to be expressed as

$$\mathbf{v}_h = v_a \hat{\mathbf{a}} + v_d \hat{\mathbf{d}}. \quad (11)$$

Applying (6), the across-track components of velocity as a function phase are

$$v_h^T \hat{\mathbf{a}} = \frac{\phi_{d,a}}{2k\delta T_a \sin \psi_a} + v_z \cot \psi_a$$

and

$$v_h^T \hat{\mathbf{d}} = \frac{\phi_{d,d}}{2k\delta T_d \sin \psi_d} + v_z \cot \psi_d. \quad (12)$$

Here the motion-only interferograms $\phi_{d,d}$ and $\phi_{d,a}$ have been unwrapped and referenced to a stationary surface so that a phase value of zero indicates no displacement. Since the basis $(\hat{\mathbf{a}}, \hat{\mathbf{d}})$ is nonorthonormal

$$v_a \neq v_h^T \hat{\mathbf{a}}$$

and

$$v_d \neq v_h^T \hat{\mathbf{d}}. \quad (13)$$

Thus, we need to determine the relation between the ad coordinates and the projections of the horizontal velocity vector on to basis vectors $\hat{\mathbf{a}}$ and $\hat{\mathbf{d}}$, which we can determine from the interferograms. These relations are derived in the Appendix. From (A5) we have

$$\begin{bmatrix} v_a \\ v_d \end{bmatrix} = \mathbf{B} \begin{bmatrix} v_h^T \hat{\mathbf{a}} \\ v_h^T \hat{\mathbf{d}} \end{bmatrix} \quad (14)$$

where

$$\mathbf{B} = \left(\frac{1}{\sin^2 \alpha} \right) \begin{bmatrix} 1 & -\cos \alpha \\ -\cos \alpha & 1 \end{bmatrix}.$$

We now need the transformation from ad to xy coordinates. Referring to Fig. 2, the ad basis vectors can be expressed as

$$\hat{\mathbf{a}} = \cos \beta \hat{\mathbf{x}} + \sin \beta \hat{\mathbf{y}}$$

and

$$\hat{\mathbf{d}} = \cos(\alpha + \beta) \hat{\mathbf{x}} + \sin(\alpha + \beta) \hat{\mathbf{y}}. \quad (15)$$

The desired coordinate transformation is then

$$\begin{bmatrix} v_x \\ v_y \end{bmatrix} = \mathbf{A} \begin{bmatrix} v_a \\ v_d \end{bmatrix} \quad (16)$$

where

$$\mathbf{A} = \begin{bmatrix} \cos \beta & \cos(\alpha + \beta) \\ \sin \beta & \sin(\alpha + \beta) \end{bmatrix}.$$

Applying (12), (14), and (16) we obtain

$$\begin{bmatrix} v_x \\ v_y \end{bmatrix} = \mathbf{AB} \begin{bmatrix} \frac{\phi_{d,a}}{2k\delta T_a \sin \psi_a} + v_z \cot \psi_a \\ \frac{\phi_{d,d}}{2k\delta T_d \sin \psi_d} + v_z \cot \psi_d \end{bmatrix}. \quad (17)$$

Applying the surface-parallel-flow assumption

$$v_z = v_x \frac{\partial}{\partial x} z_t(x, y) + v_y \frac{\partial}{\partial y} z_t(x, y) \quad (18)$$

we obtain

$$\begin{bmatrix} v_x \\ v_y \end{bmatrix} = \mathbf{AB} \begin{bmatrix} \frac{\phi_{d,a}}{2k\delta T_a \sin \psi_a} \\ \frac{\phi_{d,d}}{2k\delta T_d \sin \psi_d} \end{bmatrix} + \mathbf{ABC} \begin{bmatrix} v_x \\ v_y \end{bmatrix} \quad (19)$$

where

$$\mathbf{C} = \begin{bmatrix} \frac{\partial z_t}{\partial x} \cot \psi_a & \frac{\partial z_t}{\partial y} \cot \psi_a \\ \frac{\partial z_t}{\partial x} \cot \psi_d & \frac{\partial z_t}{\partial y} \cot \psi_d \end{bmatrix}. \quad (20)$$

Solving (19) for \mathbf{v}_h in xy coordinates yields

$$\begin{bmatrix} v_x \\ v_y \end{bmatrix} = (\mathbf{I} - \mathbf{ABC})^{-1} \mathbf{AB} \begin{bmatrix} \frac{\phi_{d,a}}{2k\delta T_a \sin \psi_a} \\ \frac{\phi_{d,d}}{2k\delta T_d \sin \psi_d} \end{bmatrix}. \quad (21)$$

This equation defines the spatially varying relation for determining the horizontal velocity vector from the unwrapped phase values. Once \mathbf{v}_h is computed, v_z is determined via (18). In the next section we apply this technique to an area in Greenland where we have data from crossing ascending and descending passes.

IV. APPLICATION TO THE RYDER GLACIER, GREENLAND

Adjacent ERS-1 tracks were widely spaced during the commissioning and ice phases of ERS-1 so that there are only a few areas in Greenland where ascending and descending tracks cross. During the tandem ERS-1/2 mission there were no gaps in coverage between adjacent tracks so that, in principle, crossing ascending and descending swaths could be collected anywhere. The majority of the Greenland data collected during the tandem mission were from descending passes. Some tandem ascending data were collected, however, so 3-D velocities can be estimated in several areas of Greenland. There are also several areas in Antarctica where this technique can be applied using data from the tandem mission.

A. Study Area and Data Set

We obtained a set of ascending and descending images (see Table I) that cover an area on Ryder Glacier in northern Greenland (see inset map in Fig. 5). This outlet glacier drains a basin of 28 300 km², which is roughly 1.7% of the inland ice area. Based on the accumulation rate data of Ohmura and Reeh [21], the total accumulation for the basin is 5.0-km³/yr water equivalent, making the Ryder a moderate-sized outlet glacier for Greenland.

An implicit assumption in the derivation of (21) is that ice flows at a steady rate during acquisition of the ascending and descending passes. This is almost always a reasonable

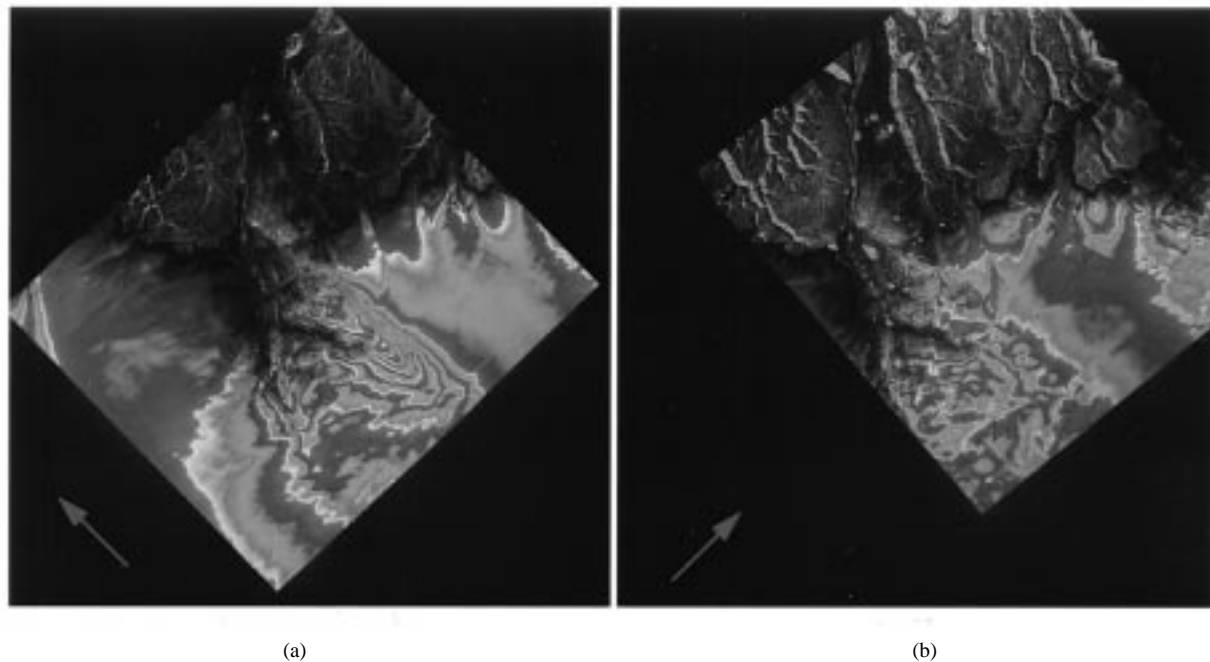


Fig. 3. (a) Descending interferogram formed from images acquired September 21–22, 1995. (b) Ascending interferogram generated using images acquired November 8–9, 1995. Both interferograms have been processed to remove the effect of topography so that phase variation is due to displacement and phase errors such as atmospheric effects. Arrows indicate across track direction.

TABLE I
INTERFEROGRAMS USED FOR ESTIMATION OF
THE FLOW FIELD OF THE RYDER GLACIER

Dates	Orbits	Frame	B_n
September 21/22, 1995	E1-21886/E2-2213	1935	41
November 8/9, 1995	E1-22577/E2-2904	1665	94
March 15/18	E1-3477/E1-3520	1935	-46
March 18/21	E1-3520/E1-3563	1935	162

assumption for ice flow, especially if the data are all acquired in winter. Kwok and Fahnestock [5] and Joughin *et al.* [7] observed steady flow rates for periods ranging from days up to nearly two years. The Ryder, however, varies its speed. A mini-surge occurred sometime in the interval from September 22–November 8, 1995 [10]. During this event, the speed on parts of the glacier appears to have increased by more than a factor of three over the normal rate. The descending data used in this study were acquired September 21–22, 1995 while the ascending data were collected November 8–9 of the same year (see Table I). These interferograms, which are shown in Fig. 3, were used to bound the period over which the mini-surge occurred [10].

The Ryder appears to have been in its normal flow mode when the September and November interferograms were acquired [10]. The mini-surge between these acquisitions, however, means that there may be differences in the flow rates observed during September and November acquisitions. We believe that any such differences are small [10]. Thus, for the purposes of demonstrating our technique, we assume that the flow rates were the same when the ascending and descending interferograms were acquired.

The difference in track directions α for the ascending and descending interferograms is 95.6° . The across-track direction of the descending interferogram is nearly aligned with the flow direction over large parts of the glacier so that there is a strong displacement signal. The prominent sets of tightly spaced, parallel fringes visible in the descending interferogram [Fig. 3(a)] are associated with velocity gradients across the shear margins. In contrast, the across-track direction of the ascending interferogram [Fig. 3(b)] is nearly orthogonal to the flow direction so that there is little effect from horizontal displacement. The often circular or “bull’s eye” patterns of fringes in this interferogram are primarily the result of vertical motion [7]. Similar patterns are also present in the descending interferogram as sensitivity to vertical displacement does not depend on track orientation.

Surface slope estimates are needed to measure velocity using (21). To determine slope, we generated a high-resolution interferometric DEM for the ice-covered areas, which required double differencing pairs of interferograms to cancel the effect of motion [5], [7]. The images used to create the DEM were acquired in March of 1992 and are listed in Table I. Nearly 1600 tie points from the KMS DEM were used to estimate the baseline. The DEM has a pixel spacing of 80 m and is shown in Fig. 4. The relative (short scale) accuracy of the DEM is on the order of a few meters [7], [8]. Baseline error and other errors may have introduced long-wavelength (i.e., greater than 10 km) errors of up to a few decameters. Fortunately, such long-wavelength errors have little effect on the accuracy of slope estimates.

Rugged topography made it difficult to unwrap the phase in the ice-free areas. As a result, we did not attempt to estimate the topography for the ice-free regions. Instead, the

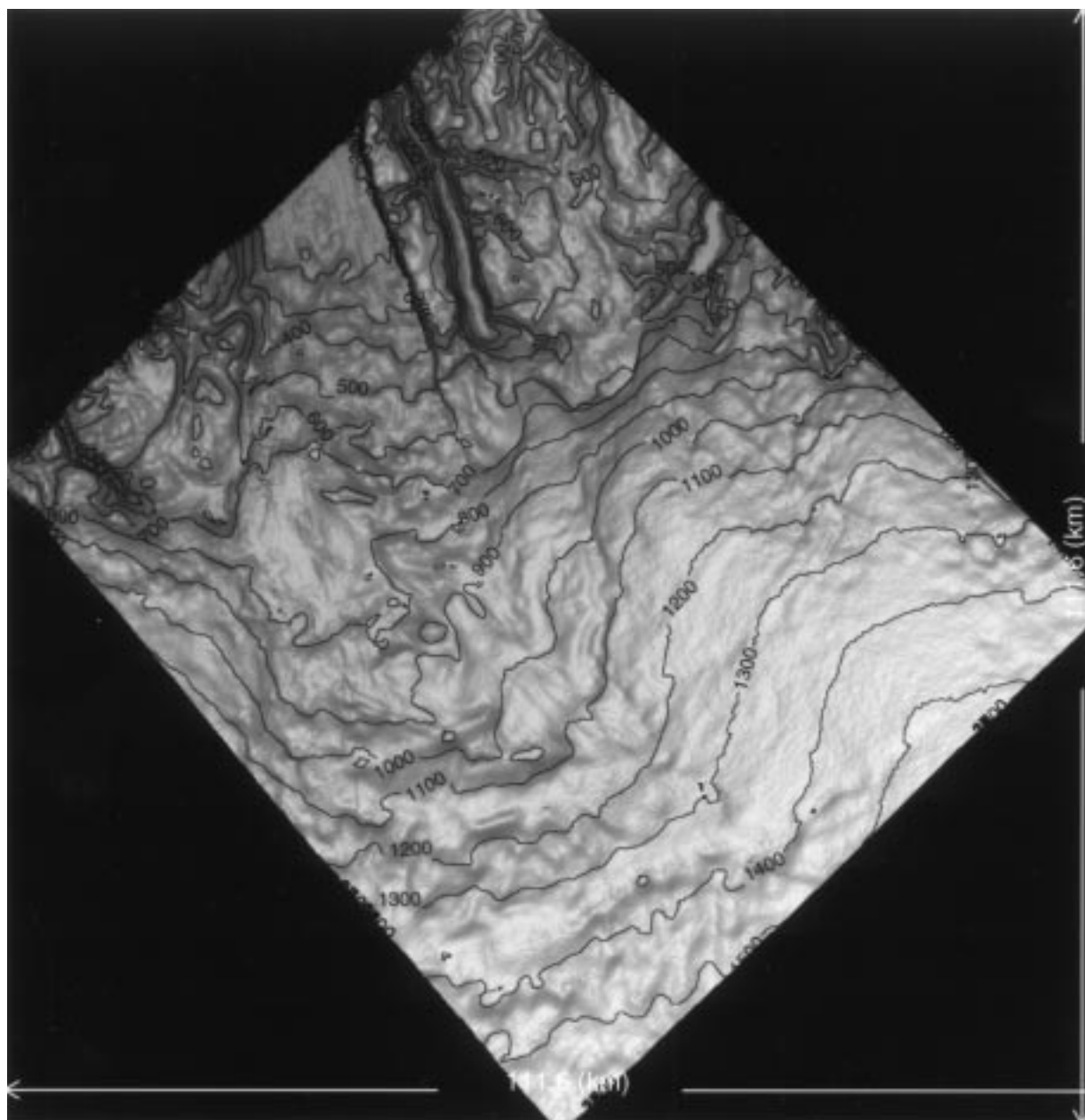


Fig. 4. High-resolution, interferometrically-derived DEM of Ryder Glacier. The DEM is shown as a shaded surface with the light source directed from above along the z -axis. Elevation contours are plotted over the surface at 100-m intervals. The images used to generate the DEM were acquired in March 1992, during the first ice phase of ERS-1.

data from these regions of the DEM shown in Fig. 4 are resampled elevations from the KMS (National Survey and Cadastre) DEM (0.5-km resolution), which was provided to us by Ekholm [22]. This does not affect our results, as we need slope data only from of the ice-covered area.

B. Coordinate System

We used the polar stereographic projection of the special sensor microwave imager (SSM/I) grid for our velocity estimates. With this coordinate system, the origin is located at the pole with the x -axis directed along 45° E and the y -axis along 135° E. In Fig. 3 and in subsequent figures, the x -coordinate increases from left to right and the y -coordinate increases from

bottom to top. The direction of true North is nearly aligned with the positive y -axis in these figures.

C. Velocity Field

To estimate velocity, we began by processing raw SAR signal data into complex, single-look images from which we created interferograms. After unwrapping the phase, we estimated the baseline using tie points from the ice-free area, which were extracted from the KMS DEM. After baseline estimation and flattening the interferograms exhibited small tilt errors, which we attributed to insufficient tie-point control in the baseline estimation procedure. To improve the results, we included tie points from the ice-covered area. Since we did not have GPS velocity measurements, we used balance-

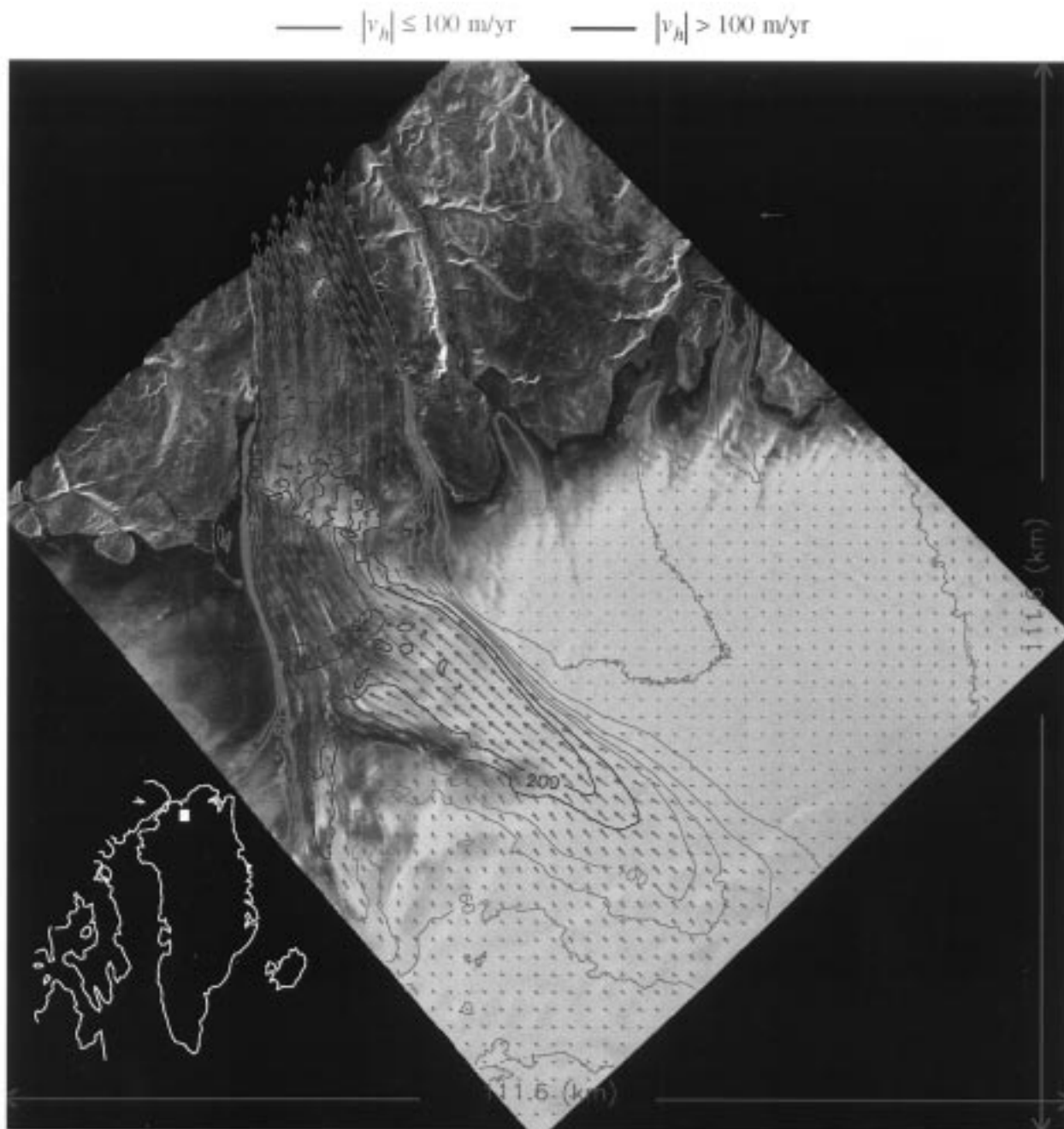


Fig. 5. Horizontal velocity field plotted over the SAR amplitude image of the Ryder Glacier. Green contours are at 20-m/yr intervals and blue contours at 50-m/yr intervals. Red arrows indicate flow direction and have length proportional to speed. The amplitude image was acquired September 21, 1995.

velocities [20], which we estimated [25] using the KMS DEM, an estimate of bed topography, and the accumulation data from Ohmura and Reeh [21]. We selected these extra tie points from the slow moving areas where balance-velocity errors are roughly a few meters per year. While not nearly as accurate as GPS-measured tie points, we believe the baseline solution determined using balance-velocity tie points is far more accurate than the solution based solely on stationary tie points from the ice-free area. The final estimates used approximately 120 tiepoints with roughly 20 points on the ice-covered area. After estimating the baseline, we cancelled the phase due to topography by differencing the interferograms

with synthetic topography-only interferograms generated from our DEM (Fig. 4). The resulting motion-only interferograms $\phi_{d,d}$ and $\phi_{d,a}$ were used to estimate velocity via (18) and (21).

The horizontal-velocity field for the Ryder is shown in Fig. 5. The Ryder has two branches, which converge at 1000 m elevation and then flow out through the Sherard Osborn Fjord, where the ice eventually goes afloat. At higher elevations the regions of converging flow associated with each of the two branches are visible while further downstream, the shear margins of the two branches become more distinct until finally, they merge to form a single tributary. In places where there are flow stripes or other indicators of flow direction, we get good

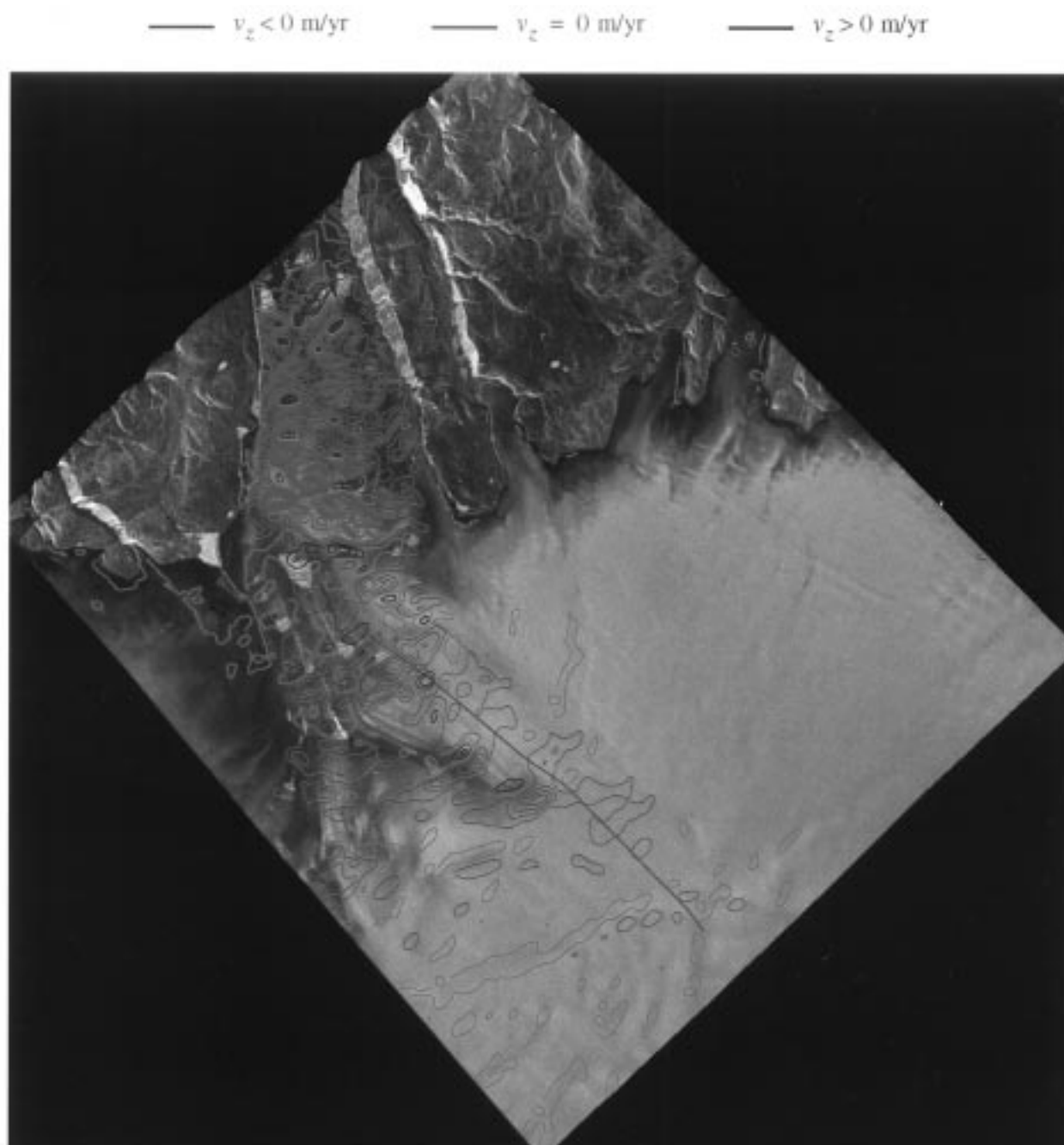


Fig. 6. Vertical component of velocity for the Ryder Glacier. Results from along the magenta profile are shown in Fig. 7. The amplitude image was acquired November 8, 1995. The contour interval is 3 m/yr.

agreement with the measured flow direction. As the ice begins to enter the exposed confines of the fjord, flow is shunted to the west by what is likely a bedrock obstacle. Once around this obstacle, the flow becomes more evenly distributed across the fjord. In addition to the Ryder flow field, the enhanced flow associated with several smaller glaciers is also visible.

The vertical component of the Ryder velocity field is shown in Fig. 6. Because the estimated vertical displacement is proportional to horizontal velocity and surface slope, there is only significant variation in regions where motion is rapid and the topography undulating. The vertical-velocity field is dominated by variation with length scales of a few ice thicknesses (i.e., a

few kilometers). The submergence/emergence contribution to the vertical component of velocity not accounted for by our estimate should vary over longer length scales and have an elevation dependence. Overall, ice flow is directed downhill so that vertical velocities are predominantly negative (red contours). There are a few areas, however, where ice must flow uphill to get over a bump (blue contours).

Different types of glaciological study require different levels of accuracy in velocity estimates. For estimation of ice discharge and for some ice dynamics studies, velocity errors of a few meters per year with length scales of a few kilometers can be considered negligible. For other ice dynamics studies the

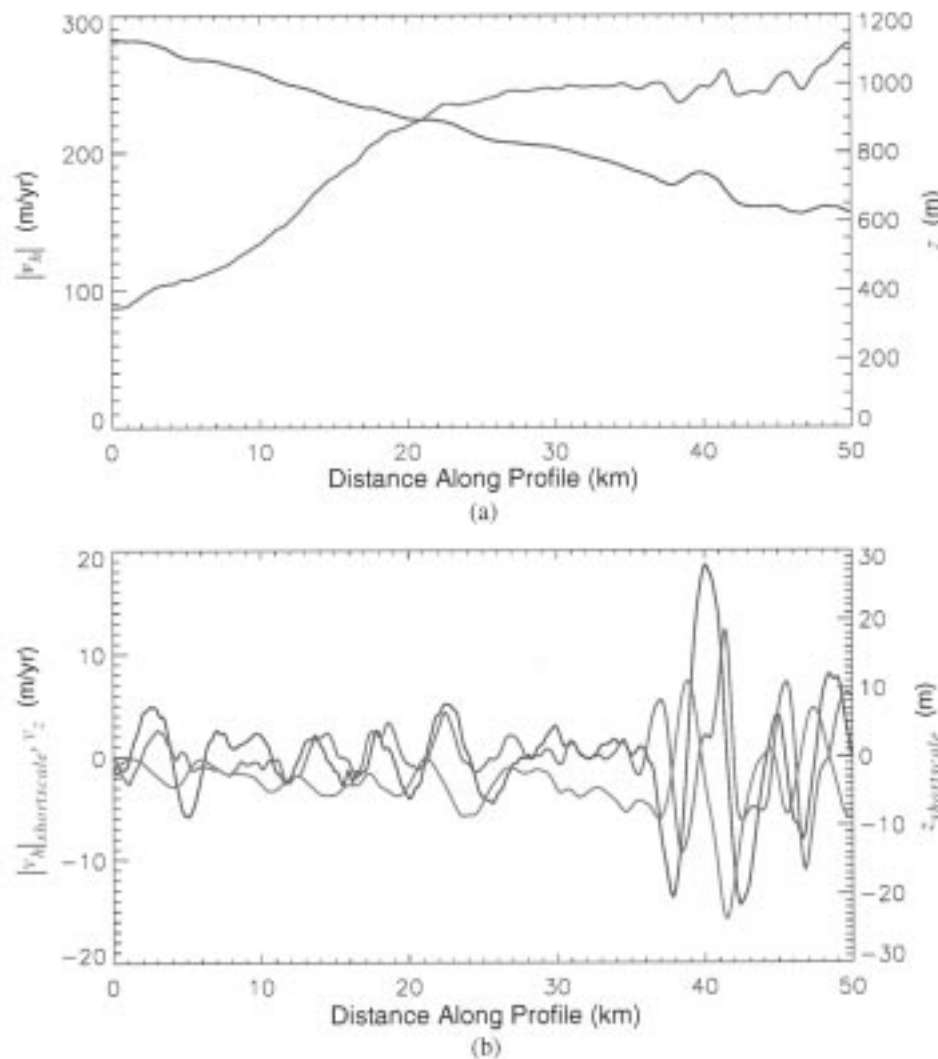


Fig. 7. (a) Profiles of horizontal speed $|v_h|$ and elevation. Profile location is indicated by a magenta line in Fig. 6. (b) Profiles of vertical velocity v_z , short-scale speed $|v_h|_{\text{shortscale}}$, and short-scale elevation $z_{\text{shortscale}}$. Short-scale variation is determined by filtering the profile to remove variation with length-scale greater than 5 km (approximately five ice thicknesses).

fine-scale details of flow are important because they represent the effects of the longitudinal stress gradients and can yield information regarding basal conditions [26]. This type of study requires a high degree of relative accuracy over length scales of a few kilometers since the amplitude of the fine-scale variability is small.

To examine the fine-scale details of our velocity estimates in greater detail, Fig. 7 shows velocity and elevation data from along the 50-km magenta profile shown in Fig. 6. The velocity data in Fig. 7(a) illustrate that the magnitude of the short-scale variation is small with respect to absolute velocity. Fig. 7(b) shows $|v_h|$ and z after high-pass filtering to remove variation with length-scale greater than 5 km (i.e., roughly five ice thicknesses). No filtering was applied to the vertical component of velocity since it exhibits little variation over length scales greater than a few kilometers.

The peaks in the small scale horizontal field velocity field occur at the tops of bumps or just on the downhill side of the bumps. The fine-scale horizontal and vertical components of velocity have similar magnitudes and are roughly 180° out of

phase. On the right side of Fig. 7(b), at the largest bump in the surface topography, one can see that the minimum in horizontal velocity corresponds to the minimum in surface slope (the maximum up glacier slope), and the maximum in velocity corresponds to the maximum slope on the down-flow side.

The results in this example seem reasonable and perhaps not overly corrupted by estimation error. Further research is needed to determine accuracy. As discussed below better characterization of the various errors and how they contribute to overall accuracy is needed. Consistent estimates from several sets of interferograms would help establish the validity of the data for the study of the fine-scale field. We also need to compare surface truth measurements of velocity with interferometric measurements to firmly establish the accuracy of our results.

D. Errors

We appear to have measured the main elements of the Ryder flow field. While our results indicate that it is possible to measure the vector velocity field for ice flow, we have not

yet established with what accuracy these measurements can be made. Analysis of the error is complicated by the fact that we do not have yet good characterizations of all sources of error. Error sources also combine in a complicated and spatially varying way, which makes analysis difficult. Finally, we have no ground truth data with which to fully validate our results. For these reasons, we limit the discussion to a description of the potential sources of error and leave a complete analysis of error as a topic for further research.

Inaccuracy in three-component velocity estimates is the result of misregistration, slope, baseline, DEM, phase-unwrapping, and phase errors. Registration error occurs when the ascending and descending interferograms and the DEM are not properly co-registered. Misregistration is caused by inaccuracy in the satellite ephemeris, along-track timing, and other data used for geolocation as well as by errors in the DEM used to remove the terrain distortion present in SAR imagery. Our data were registered with an accuracy of about 80 m for areas on the ice sheet. Ice velocity and topography typically vary over scales greater than about one ice thickness (roughly 0.5–1.2 km for the Ryder) so that misregistration is small with respect to the natural scale of variability. As a result, misregistration is typically only a factor in regions of strong phase gradients such as across shear margins and around bumps. This means that registration error primarily affects the accuracy with which we can measure the fine-scale details of the velocity field.

Accurate estimates of horizontal and vertical components of velocity require accurate surface slope estimates. The smooth nature of ice-sheet topography allows interferometric DEM's to be heavily filtered to nearly eliminate speckle as a significant source of slope error. Slopes determined from interferometric DEM's are affected by several other sources of interferometric phase errors (see below) that have length scales comparable to that of the topographic variation [7]. Multiple DEM's can be averaged to reduce slope errors [7]. Slope errors contribute to inaccuracy in measurements of fine-scale details of the velocity field.

Errors in the interferometric baseline yield residual, almost linearly varying, errors across motion-only interferograms. Baseline errors are often the largest source of error in interferometric velocity estimates [9]. A large number of accurate and well distributed tiepoints and a short interferometric baseline will help minimize these errors [9]. Since adequate tie-point information is often not available, there are many areas where baseline error can severely limit the accuracy of velocity estimates. Baseline errors have little effect on the ability to resolve subtle variations in the fine-scale velocity field.

An accurate DEM is needed to avoid residual topographic effects in the motion-only interferograms used to estimate velocity. Sensitivity of velocity estimates to DEM error is proportional to the baseline length, so using interferograms with short baseline lengths is important for keeping this type of error small. Potential long-wavelength errors in our interferometric DEM may have introduced errors of a few meters per year in our velocity estimates. DEM errors, especially for longer baselines, can affect the ability to resolve both the long- and short-wavelength features in the velocity field.

Phase-unwrapping errors lead directly to velocity errors. A phase-unwrapping program must locate discontinuities of greater than $\pm\pi$ and mark them with branch cuts so that the phase is not integrated across the discontinuity, which would otherwise introduce an error [17]. An improperly placed branch cut causes a phase discontinuity to be shifted from its actual position. Even when placed incorrectly, however, a branch cut keeps the error local instead of allowing it to become global, which would occur if no branch cut was used. Phase-unwrapping errors on ice sheets typically occur where there are strong phase gradients such as at bull's eye patterns and shear margins. Phase-unwrapping errors are reduced by eliminating strong phase gradients and improving interferometric correlation. Shortening the temporal baseline reduces phase gradients while increasing the incidence angle can further reduce the phase gradients caused by vertical displacement. Correlation can be increased by decreasing the interferometric baseline length, by reducing the temporal baseline, or by increasing the range resolution [23].

Phase noise due to speckle is often considered the limiting factor of interferometric measurements. Speckle phase noise does limit our ability to unwrap the phase correctly. Once the phase has been unwrapped, however, speckle is not a major limitation for ice sheets as the natural scale of variability allows a large amount of filtering for speckle reduction while retaining an adequate level of resolution (i.e., 100–200 m) [8]. Speckle is a more significant problem for mountain glaciers where the features of interest are much smaller.

There are several other types of phase errors in ERS interferograms that have length scales comparable to those of the measurements we wish to make so that they are not easily fixed with a simple smoothing filter. In addition to directly affecting velocity estimates, these errors also affect the accuracy of the interferometrically derived DEM's used to estimate slope and cancel topographic effects. ERS-1 interferograms from high-latitude areas often have errors that take the form of narrow (i.e., a few kilometers) streaks that sweep across the interferogram primarily in the across-track direction [8], [27]. Jezek and Rignot [27] first noticed these streaks in the correlation of an ERS-1 interferogram from western Greenland. They demonstrated that the streaks are related to high-frequency variation in the azimuth registration. If the streaks ran horizontally across (i.e., in the range direction) an interferogram, perhaps they could be explained by missing lines in the raw data. The orientation of most streaks, however, is not quite parallel to the across-track direction, making explanation of their cause difficult. The phase errors (i.e., a few tenths of a radian) introduced by these streaks are sufficient to cause velocity error of a few meters per year for a tandem ERS-1/2 pair. To the best of our knowledge these streaks have not been observed in data from outside the Kiruna ground station receiving mask. Further research is needed to establish the cause of these streak errors and whether they are unique to the ERS-1/2 SAR's.

ERS interferograms from Greenland are also subject to long-wavelength (20–100 km) phase errors (up to 10 rad) in the along-track direction [7]. These errors are possibly caused by nonlinear variation of the baseline, to clock drift [28], or to

some other cause. These large can introduce errors in velocity of up to a few decameters per year for a tandem pair. We believe this type of error accounts for, at most, a few meters per year in this study.

Goldstein [24] observed anomalous phase variation in interferograms of an area in the Mojave desert, which he attributed to additional time (phase) delay caused by turbulent water vapor in the lower atmosphere. We have observed similar features with amplitudes of a few radians in interferograms from mountainous, ice-free areas in northern Greenland [9]. Detecting such features on the ice sheet is more difficult, however, because we must differentiate them from the motion. If we had several interferograms of the same area, it would be easier to detect atmospheric effects on the ice sheet. If such features are present with lengths scales of a few kilometers as observed by Goldstein [24] and ourselves, then they will have an effect on measurements of the fine-scale velocity field. Averaging multiple estimates from different passes will help eliminate any artifacts that may be present.

V. CURRENT AND FUTURE APPLICATION

The ice and commissioning phases of ERS-1 and the tandem phase of ERS-1/2 yielded a large interferometric data set, providing descending coverage for all of Greenland and a large part of Antarctica. Unfortunately, data were acquired over only a limited area from both ascending and descending passes. An extension of the tandem mission with additional ground stations could fill in many of the gaps where there is currently no bidirectional coverage. The ERS 1/2 SAR's cannot image below 79.2° S, however, so there is no coverage for a large portion of the West Antarctic Ice Sheet. This potentially unstable ice sheet holds enough ice to raise sea-level by 6 m [28]. J-ERS-1 also provides only limited coverage of West Antarctica. RadarSat will image all of Antarctica during the RadarSat Antarctic Mapping Mission, but the 24-day temporal baseline is too long for velocity mapping, even if the radar is turned south long enough to obtain interferometric pairs. Thus, there is a need for an interferometer that can provide full Antarctic coverage.

Ice-flow rates vary from a few meters per year near the summit to several kilometers per year near the termini of large glaciers such as Jakobshavns Isbrae. The one-day temporal baseline of ERS-1/2 tandem mission is well suited for measuring ice flow in the range of about 100–1500 m/yr (note this range is a rough estimate as the glacier geometry and topography contribute greatly to the maximum velocity that can be measured). Measurement of faster motion requires a shorter temporal baseline, while estimates of slow moving ice flow benefit from longer temporal baselines. With a single SAR, the temporal baseline can be varied in integer multiples of the exact repeat period of the orbit. Thus, a short-repeat period allows a wide range of temporal baselines and the ability to measure rapidly moving ice. The tradeoff for a short repeat period is a reduction in the extent of coverage. This problem can be somewhat mitigated by the use of L-band, which allows the temporal baseline to be greater by a factor of 4 to 5 relative to C-band while maintaining the same density

of fringes due to displacement. Even with L-band, however, it is unlikely that full coverage can be achieved with a temporal baseline that is short enough to map extremely fast moving ice (i.e., greater than 2 km/yr). Fortunately, such fast moving glaciers represent a small area and they are heavily crevassed so that feature tracking can be used to measure their velocity.

Short baselines are important for obtaining accurate ice velocity estimates [9]. Long baselines also are needed to obtain the good height accuracy necessary for keeping slope error small. The lengths of a large percentage of the ERS-1/2 tandem baselines are suboptimal for estimation of either topography or velocity. Future missions should be designed with the capability to maintain the interferometric baseline in a specified range (both short and long) to allow efficient use of data in ice-sheet [9] and other types of deformation research [29].

As described above several types of nonspeckle phase errors affect the accuracy of ERS-1/2 estimates. The long-wavelength and streak errors may be unique to ERS-1/2, but atmospheric anomalies will impact any future repeat-pass interferometer, regardless of frequency [24]. These errors vary independently from interferogram to interferogram (assuming no common images) so that they can be reduced by averaging several estimates. Slope errors can be reduced in a similar fashion by averaging several DEM's to improve height accuracy. This approach can not be applied to much of the current ERS-1/2 tandem data set as typically there were only one or two pairs collected along each track. Any interferometry mission or extension of the tandem mission should be planned so that enough pairs are collected to achieve the desired accuracy via averaging of multiple estimates.

VI. CONCLUSIONS

We have demonstrated that interferograms from ascending and descending passes can be combined with surface slope information to estimate the 3-D ice-flow velocity field. Further research is needed to determine how accurately the fine-scale details of the velocity field can be determined. Application of the technique is currently limited to a small percentage of the area covered by the Greenland and Antarctic Ice Sheets where both ascending and descending data were collected. Data from existing and future missions, however, hold great promise for advancing our knowledge of ice sheet dynamics and mass balance.

APPENDIX

COORDINATES FOR TWO-DIMENSIONAL, NON-ORTHONORMAL BASIS IN TERMS OF ACROSS-TRACK VELOCITY COMPONENTS

Consider two orthonormal xy -coordinate systems rotated with respect to each other as shown in Fig. 8. For an arbitrary vector \mathbf{v}_h we can relate the coordinates in one system to those in the other by

$$\begin{aligned} v_{x_1} &= v_{x_2} \cos \alpha - v_{y_2} \sin \alpha \\ v_{y_1} &= v_{x_2} \sin \alpha + v_{y_2} \cos \alpha \\ v_{x_2} &= v_{x_1} \cos \alpha + v_{y_1} \sin \alpha \\ v_{y_2} &= -v_{x_1} \sin \alpha + v_{y_1} \cos \alpha, \end{aligned} \quad (A1)$$

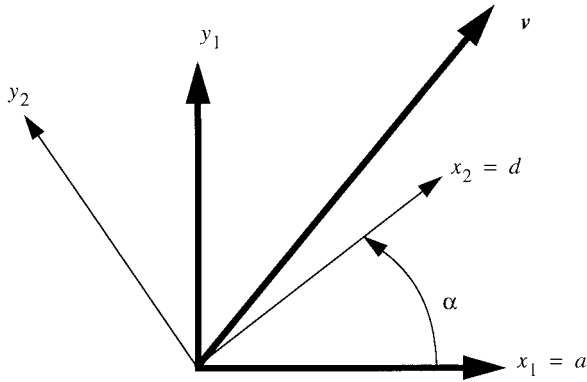


Fig. 8. Definition of coordinates, vectors, and rotations used in deriving nonorthonormal basis.

After some algebra we obtain

$$v_{y1} = \frac{v_{x2}}{\sin \alpha} - v_{x1} \frac{\cos \alpha}{\sin \alpha}. \quad (A2)$$

Similarly we obtain

$$\hat{y}_1 = -\left(\frac{\cos \alpha}{\sin \alpha}\right)\hat{x}_1 + \left(\frac{1}{\sin \alpha}\right)\hat{x}_2. \quad (A3)$$

Substituting (A2) and (A3) into

$$v_h = v_{x1}\hat{x} + v_{y1}\hat{y} \quad (A4)$$

and letting $\hat{a} = \hat{x}_1$ and $\hat{d} = \hat{x}_2$ we obtain

$$v_h = v_a\hat{a} + v_d\hat{d} \quad (A5)$$

where

$$v_a = \left(\frac{v_h^T \hat{a} - v_d^T \hat{d} \cos \alpha}{\sin^2 \alpha} \right)$$

and

$$v_d = \left(\frac{v_h^T \hat{d} - v_a^T \hat{a} \cos \alpha}{\sin^2 \alpha} \right).$$

This gives the coordinates in the nonorthonormal basis in terms of the projections of the horizontal velocity vector onto the basis vectors.

ACKNOWLEDGMENT

The authors thank S. Ekholm of the National Survey and Cadastre, Copenhagen, Denmark, for providing us with the DEM. We also wish to thank C. Werner of the Jet Propulsion Laboratory for providing us with a SAR processor for the raw signal data.

REFERENCES

- [1] T. A. Scambos, M. J. Dutkiewicz, J. C. Wilson, and R. A. Bindschadler, "Application of image cross-correlation to the measurement of glacier velocity using satellite image data," *Remote Sens. Environ.*, vol. 42, pp. 177–186, 1992.
- [2] M. Fahnestock, R. Bindschadler, R. Kwok, and K. Jezek, "Greenland ice sheet surface properties and ice dynamics from ERS-1 SAR imagery," *Science*, vol. 262, pp. 1530–1534, 1993.
- [3] R. M. Goldstein, H. Engelhardt, B. Kamb, and R. M. Frolich, "Satellite radar interferometry for monitoring ice sheet motion: Application to an Antarctic ice stream," *Science*, vol. 262, pp. 1525–1530, 1993.
- [4] Ph. Hartl, K. H. Thiel, X. Wu, Ch. Doake, and J. Sievers, "Application of SAR interferometry with ERS-1 in the Antarctic," *Earth Observ. Quart.*, no. 43, pp. 1–4, 1995.
- [5] R. Kwok and M. A. Fahnestock, "Ice sheet motion and topography from radar interferometry," *IEEE Trans. Geosci. Remote Sensing*, vol. 34, pp. 189–200, Jan. 1996.
- [6] I. R. Joughin, D. P. Winebrenner, and M. A. Fahnestock, "Observations of ice-sheet motion in Greenland using satellite radar interferometry," *Geophys. Res. Lett.*, vol. 22, no. 5, pp. 571–574, 1995.
- [7] I. Joughin, D. Winebrenner, M. Fahnestock, R. Kwok, and W. Krabill, "Measurement of ice-sheet topography using satellite radar interferometry," *J. Glaciology*, vol. 42, no. 140, pp. 10–22, 1996.
- [8] I. R. Joughin, "Estimation of ice sheet topography and motion using interferometric synthetic aperture radar," Ph.D. dissertation, Univ. of Washington, Seattle, Mar. 1995.
- [9] I. Joughin, R. Kwok, and M. Fahnestock, "Estimation of ice sheet motion using satellite radar interferometry: Method and error analysis with application to the Humboldt Glacier, Greenland," *J. Glaciology*, vol. 42, no. 142, pp. 564–575, 1996.
- [10] I. Joughin, S. Tulaczyk, M. Fahnestock, and R. Kwok, "A mini-surge on the Ryder Glacier, Greenland observed via satellite radar interferometry," *Science*, vol. 262, pp. 1525–1530, 1996.
- [11] E. Rignot, K. C. Jezek, and H. G. Sohn, "Ice flow dynamics of the Greenland ice sheet from SAR interferometry," *Geophys. Res. Lett.*, vol. 22, no. 5, pp. 575–578, 1995.
- [12] E. Rignot, "Tidal flexure, ice velocities, and ablation rates of Petermann Gletscher, Greenland," *J. Glaciology*, vol. 42, no. 142, pp. 476–485, 1996.
- [13] E. Rignot, R. Forster, and B. Isacks, "Radar interferometric observations of Glacier San Rafael, Chile," *J. Glaciology*, vol. 42, no. 141, pp. 279–291, 1996.
- [14] P. W. Vachon, D. Geudtner, K. Mattar, A. L. Gray, M. Brugman, and I. Cumming, "Differential SAR interferometry measurements of Athabasca and Saskatchewan glacier flow rate," *Can. J. Remote Sensing*, vol. 22, no. 3, pp. 287–296, Sept. 1996.
- [15] D. R. Fatland, "Analysis of Bagley Ice Field glacier dynamics using differential spaceborne radar interferometry," in *Proc. AGU Fall Meeting*, San Francisco, CA, 1995.
- [16] H. A. Zebker, S. N. Madsen, J. Martin, K. B. Wheeler, T. Miller, Y. Lou, G. Alberti, S. Vetrilla, and A. Cucci, "The TOPSAR interferometric radar topographic mapping instrument," *IEEE Trans. Geosci. Remote Sensing*, vol. 30, pp. 933–940, Sept. 1992.
- [17] R. M. Goldstein, H. A. Zebker, and C. L. Werner, "Satellite radar interferometry: Two-dimensional phase unwrapping," *Radio Sci.*, vol. 23, no. 4, pp. 713–720, 1988.
- [18] H. A. Zebker, C. L. Werner, P. A. Rosen, and S. Hensley, "Accuracy of topographic maps derived from ERS-1 interferometric radar," *IEEE Trans. Geosci. Remote Sensing*, vol. 32, pp. 823–836, July 1994.
- [19] W. H. Press, S. A. Teukolsky, W. T. Vetterling, and B. P. Flannery, *Numerical Recipes in C, the Art of Scientific Computing*, 2nd ed. Cambridge, U.K.: Cambridge Univ. Press, 1992.
- [20] W. S. B. Paterson, *The Physics of Glaciers*, 3rd ed. Oxford, U.K.: Pergamon, 1994.
- [21] A. Ohmura and N. Reeh, "New precipitation and accumulation maps for Greenland," *J. Glaciology*, vol. 37, no. 125, 1991.
- [22] S. Ekholm, "A full coverage, high-resolution, topographic model of Greenland, computed from a variety of digital elevation data," *J. Geophys. Res.*, vol. B10, no. 21, pp. 961–972, 1996.
- [23] H. Zebker and J. Villasenor, "Decorrelation in interferometric radar echoes," *IEEE Trans. Geosci. Remote Sensing*, vol. 30, pp. 950–959, Sept. 1992.
- [24] R. M. Goldstein, "Atmospheric limitations to repeat-track radar interferometry," *Geophys. Res. Lett.*, vol. 22, no. 18, pp. 2517–2520, 1995.
- [25] I. Joughin, M. Fahnestock, and R. Kwok, "Balance velocities for the Greenland Ice Sheet," in preparation.
- [26] C. Raymond and H. Gudmundsson, personal communication.
- [27] K. Jezek and E. Rignot, "Katabatic wind processes on the Greenland ice sheet," in *Proc. AGU Fall Meeting*, San Francisco, CA, 1994.
- [28] R. B. Alley and I. M. Whillans, "Changes in the West Antarctic Ice Sheet," *Science*, vol. 254, pp. 959–963, 1991.
- [29] P. Rosen, C. Werner, J. B. Minster, and H. Zebker, "Radar interferometry satellite mission concepts for Earth change and hazards observation," in *Proc. AGU Fall Meeting*, San Francisco, CA, 1996.

Ian R. Joughin (S'89–M'97) received the B.S.E.E. degree in 1986 and the M.S.E.E. degree in 1990, both from the University of Vermont, Burlington, and the Ph.D. degree from the University of Washington, Seattle, in 1994. His doctoral dissertation concerned the remote sensing of ice sheets using satellite radar interferometry.

From 1986 to 1988, he was with Green Mountain Radio Research, Burlington, VT, where he worked on signal-processing algorithms and hardware for a VLF through-the-earth communications system. From 1991 to 1994, he was a Research Assistant at the Polar Science Center, Applied Physics Laboratory, University of Washington. From May 1995 to May 1996, he was a Postdoctoral Researcher with the Jet Propulsion Laboratory (JPL), California Institute of Technology, Pasadena. He is currently a Member of the Technical Staff at JPL. His research interests include microwave remote sensing, SAR interferometry, and the remote sensing of polar regions.

Dr. Joughin is a member of Tau Beta Pi and the American Geophysical Union.



Ronald Kwok (S'82–M'84) received the B.S. degree (summa cum laude) from Texas A & M University, College Station, in 1976 and the Ph.D. degree from Duke University, Durham, NC, in 1980.

He was a postdoctoral fellow at the University of British Columbia, Vancouver, B.C., Canada, in 1981. In 1985, he joined the Radar Science and Engineering Section at the Jet Propulsion Laboratory, California Institute of Technology, Pasadena. He is currently a Technical Supervisor of the Polar Remote Sensing Group responsible for research and

development of analysis and processing techniques for active and passive microwave data of the polar regions. His interest includes the mass balance of the Arctic Ocean sea ice and mapping of Antarctica using satellite radar interferometry.

Dr. Kwok is a member of the American Geophysical Union, American Meteorological Society, Electromagnetics Academy, Tau Beta Pi, Phi Kappa Phi, and Eta Kappa Nu.

Mark A. Fahnestock received the B.Sc. degree from the University of Rochester, Rochester, NY, in 1984 and the Ph.D. degree from the California Institute of Technology, Pasadena, in 1991.

He is a Glaciologist working at the Joint Center for Earth System Science, Department of Meteorology, University of Maryland, College Park. Trained as a geologist, his research interests include dynamics of ice sheets and glaciers and the response of ice sheets to climate change. This research is based on both field work and remote sensing data.